A scale-dependent dynamic model for large-eddy simulation: application to a neutral atmospheric boundary layer

By FERNANDO PORTÉ-AGEL[1,3],
CHARLES MENEVEAU[2,3] AND MARC B. PARLANGE[1,3]

[1]Department of Geography and Environmental Engineering,

[2]Department of Mechanical Engineering,

[3]Center for Environmental and Applied Fluid Mechanics, The Johns Hopkins University,
Baltimore, MD 21218, USA

A scale-dependent dynamic subgrid-scale model for large-eddy simulation of turbulent flows is proposed. Unlike the traditional dynamic model, it does not rely on the assumption that the model coefficient is scale invariant. The model is based on a second test-filtering operation which allows us to determine from the simulation how the coefficient varies with scale. The scale-dependent model is tested in simulations of a neutral atmospheric boundary layer. In this application, near the ground the grid scale is by necessity comparable to the local integral scale (of the order of the distance to the wall). With the grid scale and/or the test-filter scale being outside the inertial range, scale invariance is broken. The results are compared with those from (*a*) the traditional Smagorinsky model that requires specification of the coefficient and of a wall damping function, and (*b*) the standard dynamic model that assumes scale invariance of the coefficient. In the near-surface region the traditional Smagorinsky and standard dynamic models are too dissipative and not dissipative enough, respectively. Simulations with the scale-dependent dynamic model yield the expected trends of the coefficient as a function of scale and give improved predictions of velocity spectra at different heights from the ground. Consistent with the improved dissipation characteristics, the scale-dependent model also yields improved mean velocity profiles.

1. Introduction

Large-eddy simulation (LES) has become an important tool for the study of turbulent transport in environmental flows (Deardorff 1974; Moeng 1984; Moeng & Wyngaard 1984; Shaw & Schumann 1992; Mason 1994) and engineering flows (Lesieur & Métais 1996; Piomelli 1999). LES explicitly resolves the flow at scales larger than a certain scale $\varDelta$, while the scales smaller than $\varDelta$ are parameterized. Effective equations for the large scales are derived by spatially filtering the original Navier–Stokes equations at the grid scale $\varDelta$ (filtered variables are denoted henceforth by a tilde). The effect of the subgrid-scale (SGS) motion is represented by the divergence of the SGS stress. The SGS stress is defined as

$$\tau_{ij} = \widetilde{u_i u_j} - \widetilde{u}_i \widetilde{u}_j \tag{1.1}$$

and it must be closed in terms of the resolved field $\widetilde{u}_i$.

An important development in SGS modelling occurred with the formulation of the Germano identity (Germano *et al.* 1991). By relating stresses at different scales, the indentity allows model coefficients to be determined from the resolved scales during LES. One of the major assumptions of this dynamic approach is scale similarity, i.e. that model coefficients are invariant under scale transformation (Meneveau & Katz 2000). While this is a reasonable assumption if Δ pertains to an idealized inertial range of turbulence, it is not expected to hold if Δ falls near a transition scale (denoted below by Δ_t) where more complicated physics may occur. For example, in certain parts of the flow the grid scale may approach the integral scale. This limit is of relevance when LES approaches the Reynolds-averaged Navier–Stokes formulation. In particular, such a situation occurs in LES of wall-bounded flows where the integral scale is of the order of the distance to the wall, z. If the simulation does not resolve the viscous sublayer, the first few cells near the wall have a grid scale on the order of the local integral scale. Thus, at a scale $\Delta_t \sim z$ one expects a transition behaviour, and possibly inaccurate results from the traditional dynamic model. In this flow in the near-wall region the subgrid stress is a significant fraction of the total stress and hence the accuracy of the results is particularly sensitive to the SGS model.

In §2, applications of the standard dynamic model for LES of a neutral atmospheric boundary layer (ABL) are presented that illustrate the difficulty associated with the assumption of scale-invariance. Comparisons with the non-dynamic Smagorinsky model are also presented.

Other examples where one may expect scale dependence of model coefficients include the following. In turbulence undergoing rapid strains of magnitude S, a transition length $\Delta_t \sim S^{-3/2}\varepsilon^{1/2}$ appears (ε is the dissipation rate). Roughly speaking, eddies larger than $S^{-3/2}\varepsilon^{1/2}$ are rapidly distorted but have no time to adjust dynamically, while smaller eddies can respond faster via nonlinear interactions (Smith & Yakhot 1993; Liu, Katz & Meneveau 1999). In stratified flows, a transition behaviour of the coefficient is expected near the Ozmidov scale, i.e. $\Delta_t \sim N^{-3/2}\varepsilon^{1/2}$, where N is the Brunt–Väisälä frequency (Ozmidov 1975; Canuto & Minotti 1993). Eddies of size Δ_t and larger can lose kinetic energy to gravity waves, which must be accounted for in the SGS model if the grid scale Δ is of size Δ_t or larger. When LES approaches direct numerical simulation (DNS), the model coefficient varies when the grid scale approaches the Kolmogorov scale η, i.e. the transition occurs near $\Delta_t \sim \eta$ (Voke 1996; Meneveau & Lund 1997; Pope 2000). For each of these cases, one expects scale dependence of the model coefficient near Δ_t and thus a violation of the central assumption of the dynamic model. Moreover, in complex flow conditions, one does not necessarily know *a priori* how the coefficient changes with scale, e.g. whether it increases or decreases with decreasing scale.

The aim of the present paper is to introduce a generalization of the dynamic model that relaxes the assumption of strict scale invariance. Briefly, the methodology is based on introducing a secondary test filter that, in addition to the traditional test filter, is used to determine both the coefficient and how it changes across scales. The basic idea of the scale-dependent dynamic model is presented in §3. Section 4 presents applications of the scale-dependent dynamic model to non-sub-layer-resolving LES of the neutral atmospheric boundary layer. Section 5 presents the conclusions.

The focus of this paper is on the dynamic Smagorinsky model. Other models have been proposed in the literature. For example, in order to account for backscatter, inclusion of stochastic models was proposed (Mason & Thomson 1992; Schumann 1995). Another more deterministic approach to the problem is the use of a two-part eddy-viscosity model in which the mean and fluctuating shear are treated separately.

This approach was first proposed by Schumann (1975) and used in simulations of channel flow by Grotzbach & Schumann (1977), Schumann, Grotzbach & Kleiser (1980) and Moin & Kim (1982), and more recently in simulations of the ABL by Sullivan, McWilliams & Moeng (1994) and Khanna & Brasseur (1997). Another variant of the eddy-viscosity model, which does not require the assumption of local equilibrium, is to express the eddy viscosity in terms of the subgrid turbulent kinetic energy (TKE) and solve an additional transport equation (Moeng 1984; Nieuwstadt & Brost 1986; Schmidt & Schumann 1989). As reviewed in Meneveau & Katz (2000), it has been argued (Piomelli, Yu & Adrian 1996; Horiuti 1997) that similarity and mixed models (see e.g. Bardina, Ferziger & Reynolds 1980; Liu, Meneveau & Katz 1994; Sarghini, Piomelli & Balaras 1999) can reproduce the SGS physics in turbulent boundary layers more accurately than eddy-viscosity models alone.

For reasons of clarity and in order not to confuse effects, in this paper we restrict attention to the dynamic Smagorinsky model and its generalization that allows for scale dependence. Clearly, however, further improvements may be obtained in the future by considering scale-dependent dynamic reformulations of the other base models mentioned here. Another important issue in LES that does not resolve the viscous sublayer is the need to prescribe the shear stress at the wall. Again, in order to avoid confusing effects in this work we will use the most standard approach based on a local log-law (Moeng 1984).

2. The traditional Smagorinsky and standard dynamic models

2.1. *Smagorinsky model*

The traditional Smagorinsky model (Smagorinsky 1963) for the deviatoric part of the stress is as follows:

$$\tau_{ij} - \tfrac{1}{3}\delta_{ij}\tau_{kk} = -2v_T\widetilde{S}_{ij}, \qquad (2.1)$$

where $\widetilde{S}_{ij} = \tfrac{1}{2}(\partial\widetilde{u}_i/\partial x_j + \partial\widetilde{u}_j/\partial x_i)$ is the resolved strain-rate tensor and v_T is the eddy viscosity given by

$$v_T = [C_S \varDelta]^2 |\widetilde{S}|. \qquad (2.2)$$

Here $|\widetilde{S}| = (2\widetilde{S}_{ij}\widetilde{S}_{ij})^{1/2}$ is the magnitude of the resolved strain-rate tensor, $\varDelta$ is the filter width, and C_S is a non-dimensional parameter called the Smagorinsky coefficient. Lilly (1967) determined that, for homogeneous isotropic turbulence with cutoff in the inertial subrange and $\varDelta$ equal to the grid size, $C_S \approx 0.17$. In the presence of mean shear, however, this value is found to cause excessive damping of large-scale fluctuations. Results from simulations show that the optimal value of C_S decreases with increasing mean shear. For example in simulations of channel flow, Deardorff (1970) and Piomelli, Moin & Ferziger (1988) use $C_S = 0.1$; Bardina (1983) finds an optimum value of 0.09, and Moin & Kim (1982) use $C_S = 0.065$. Although the exact cause for the observed dependence of C_S on mean shear is not completely understood, in general it is observed that a decrease in the Smagorinsky coefficient coincides with an increase in anisotropy in both the resolved and SGS velocities (Horiuti 1993). The Smagorinsky coefficient also varies with grid mesh aspect ratio (Scotti, Meneveau & Lilly 1993).

Application of the Smagorinsky model in LES of high-Reynolds-number wall-bounded turbulent flows, including the ABL, has involved the use of wall damping functions. As the ground is approached, the SGS mixing length $\lambda = C_S\varDelta$ is made to decrease by means of an *ad-hoc* expression in order to smoothly merge with

the expected $\lambda \sim z$ behaviour (Mason 1989). Mason & Thomson (1992) propose a matching function of the form

$$\frac{1}{\lambda^n} = \frac{1}{\lambda_o^n} + \frac{1}{\{\kappa(z + z_o)\}^n},$$ (2.3)

where κ (≈ 0.4) is the von Kármán constant, $\lambda_o = C_o \Delta$ is the length far from the wall, z_o is the roughness length, and n is an adjustable parameter. They apply this formulation with different values of C_o (ranging from about 0.1 to 0.3) and n (1, 2, and 3), and show that for all cases the model is too dissipative, especially near the surface. Energy spectra decay too rapidly at high wavenumbers, and the model yields unrealistic mean velocity profiles in the lower part of the boundary layer, where the vertical gradients of the streamwise velocity typically depart by up to 100% from the well-established logarithmic profile under neutral conditions. This leads to an overestimation of the mean streamwise velocity throughout the domain.

Andrén *et al.* (1994) have performed an extensive comparison of various LES codes using the traditional Smagorinsky model (with wall damping) and other eddy-viscosity models that use a prognostic equation for the subgrid-scale kinetic energy. They confirm that the spectra as a function of streamwise wavenumber show excessive damping starting at wavenumbers significantly smaller than the cutoff wavenumber. Also, the log layer is not well reproduced near the wall.

2.2. *Standard dynamic model*

The dynamic model (Germano *et al.* 1991) avoids, in principle, the need for *a priori* specification and consequent tuning of the coefficient because it is evaluated directly from the resolved scales in an LES. The approach is based on the Germano identity

$$L_{ij} = T_{ij} - \overline{\tau}_{ij} = \overline{\widetilde{u_i} \widetilde{u}_j} - \widetilde{\overline{u}}_i \widetilde{\overline{u}}_j,$$ (2.4)

where $T_{ij} = \widetilde{\overline{u_i u_j}} - \widetilde{\overline{u}}_i \widetilde{\overline{u}}_j$ is the stress at a test-filter scale $\overline{\Delta}$ (typically $\overline{\Delta} = 2\Delta$) and L_{ij} is the 'resolved stress' tensor that can be evaluated based on the resolved scales. Applying the dynamic procedure to the Smagorinsky model, T_{ij} is determined by

$$T_{ij} - \tfrac{1}{3}\delta_{ij} T_{kk} = -2(C_S(\overline{\Delta})\overline{\Delta})^2 |\widetilde{\overline{S}}| \widetilde{\overline{S}}_{ij}.$$ (2.5)

Substitution of (2.1) and (2.5) into (2.4), in addition to the crucial assumption of scale invariance,

$$C_S(\Delta) = C_S(\overline{\Delta}) = C_S,$$ (2.6)

leads to the system

$$L_{ij} - \tfrac{1}{3}\delta_{ij} L_{kk} = C_S^2 M_{ij},$$ (2.7)

where

$$M_{ij} = 2\Delta^2 (\overline{|\overline{S}| \overline{S}_{ij}} - 4|\widetilde{\overline{S}}| \widetilde{\overline{S}}_{ij}) \quad \text{for} \quad \overline{\Delta} = 2\Delta.$$ (2.8)

Minimizing the error associated with the use of the Smagorinsky model in the Germano identity (equation (2.7)) over all independent tensor components (Lilly 1992) as well as over some averaging region of statistical homogeneity (Ghosal *et al.* 1995) or fluid pathlines (Meneveau, Lund & Cabot 1996), results in

$$C_S^2 = \frac{\langle L_{ij} M_{ij} \rangle}{\langle M_{ij} M_{ij} \rangle}.$$ (2.9)

In this derivation a spatially homogeneous filter is assumed. This avoids additional

complications that arise for non-homogeneous filters, for which differentiation and filtering do not commute in the momentum equation (see Ghosal & Moin 1995).

The dynamic model has, so far, not been applied extensively to simulations of atmospheric boundary layers. Balaras, Benocci & Piomelli (1995) have used the dynamic model in LES of channel flow in which the viscous sublayer is not resolved, and find that it accounts for wall damping without the need for any *ad hoc* damping function. However, as summarized in §1, in such high-Reynolds-number LES, the assumption of scale invariance (equation (2.6)) may not hold near the wall. Indeed, in §2.4 it is shown that the results obtained from LES of the ABL using the standard (scale-independent) dynamic model are inconsistent with the assumption of scale invariance. Notice that already the *ad hoc* damping function in (2.3) can be rewritten as a function of z/Δ:

$$C_S = \left(C_o^{-n} + \left\{ \kappa \left(\frac{z}{\Delta} + \frac{z_o}{\Delta} \right) \right\}^{-n} \right)^{-1/n}, \tag{2.10}$$

i.e. at a fixed height above the ground, the coefficient is scale dependent.

2.3. *Numerical simulations*

We implement the traditional Smagorinsky and standard dynamic models, as presented in §§2.1 and 2.2, in the simulation of a neutrally stable (no convective forcing) atmospheric boundary layer. We use a modified version of the LES code described in Albertson & Parlange (1999). The code solves the filtered Navier–Stokes equations written in rotational form (Orszag & Pao 1974)

$$\frac{\partial \widetilde{u}_i}{\partial t} + \widetilde{u}_j \left(\frac{\partial \widetilde{u}_i}{\partial x_j} - \frac{\partial \widetilde{u}_j}{\partial x_i} \right) = -\frac{\partial \widetilde{p}^*}{\partial x_i} - \frac{\partial \tau_{ij}}{\partial x_j} + F_i, \tag{2.11}$$

where t is time, $\widetilde{u}_i$ is the instantaneous resolved velocity in the i-direction, $\widetilde{p}^* = \widetilde{p}/\rho + \frac{1}{2}\widetilde{u}_i^2$ is the modified pressure divided by density ρ, τ_{ij} is the SGS stress tensor, and F_i is a forcing term. Specifically, F_i is a constant pressure gradient in the streamwise direction that drives the flow. Since the Reynolds number of the ABL is high and no near-ground viscous processes are resolved, the viscous term is neglected in the momentum equation. Note that the gradient of resolved kinetic energy has been included in the pressure gradient. The dynamic pressure field is obtained by solving the Poisson equation that results from taking the divergence of the momentum equation and applying the continuity equation. Since this paper focuses on the case of neutral stability conditions, no additional terms are used to account for buoyancy effects. Also no Coriolis forces have been included.

The simulated ABL is horizontally homogeneous. The horizontal directions are discretized pseudo-spectrally, while vertical derivatives are approximated with second-order central differences. The grid planes are staggered in the vertical with the first vertical velocity plane at a distance $\Delta_z = L_z/(N_z - 1)$ from the surface, and the first horizontal velocity plane $\Delta_z/2$ from the surface. The vertical height of the computational domain is $L_z = 1000\,\mathrm{m}$, which corresponds to the height of the boundary layer (H), and the horizontal dimensions of the simulated volume are $L_x = L_y = 2\pi L_z$. The domain is divided into N_x, N_y, and N_z uniformly spaced grid points. Near the ground, the expected logarithmic mean velocity profile involves a rapidly increasing vertical gradient. In order to reduce the error incurred by using a finite-difference approach to compute the vertical derivative in the $\widetilde{u}_3 \partial \widetilde{u}_1/\partial z$ convective term, at the first node $z = \Delta_z/2$ a correction factor is included in the formulation

as described in the Appendix. This improvement is introduced because the vertical derivative of an expected logarithmic mean profile diverges at the wall, causing some errors in the finite-difference approximation.

The pseudo-spectrally evaluated convective terms are dealiased by padding and truncation using the 3/2 rule (Orszag 1970). A rigorous dealiasing of these terms is necessary, since aliasing errors affect the smallest resolved scales, which are used by the dynamic procedure to compute the model coefficient. As in previous applications of the traditional dynamic model in channel flow (e.g. Germano *et al.* 1991; Piomelli 1993), the variables are filtered in Fourier space by employing a sharp cutoff filter at wavenumbers larger than the filter scale. The grid filter and the two test filters are two-dimensional low-pass filters that take advantage of the spectral nature of the code in the horizontal directions.

Finite differencing in the vertical requires boundary conditions at the surface and upper boundaries. The upper boundary has a stress-free condition, i.e. $\partial \widetilde{u}_1 / \partial z = \partial \widetilde{u}_2 / \partial z = 0$. At the surface, the instantaneous wall stress is related to the velocity at the first vertical node through the application of the Monin–Obukhov similarity theory (Businger *et al.* 1971). Although this theory was developed for mean quantities, it is common practice in LES of atmospheric flows to use it for instantaneous fields (Moeng 1984) as follows:

$$\tau_{i3} \mid_w = -u_*^2 [\widetilde{u}_i / U(z)] = -\left[\frac{U(z)\kappa}{\{\ln(z/z_o) - \Psi_M\}} \right]^2 [\widetilde{u}_i / U(z)] \quad (i = 1, 2), \qquad (2.12)$$

where $\tau_{i3} \mid_w$ is the instantaneous wall stress, u_* is the friction velocity, z_o is the roughness length, κ is the von Kármán constant ($\kappa = 0.4$), and Ψ_M is the stability correction for momentum. In the case of neutral stability, $\Psi_M = 0$. $U(z) = \langle \widetilde{u}_1 \rangle$ is the mean resolved horizontal velocity, and $\widetilde{u}_i$ is the instantaneous resolved velocity, both at a height z (in our case, $z = \Delta_z / 2$). This classical parameterization of the boundary condition neglects effects of pressure gradients, unsteadiness, streamline curvature, etc., which occur in the instantaneous LES fields. We use it nonetheless since no universally agreed upon improved wall-stress model has been developed to date, and in order not to confuse effects with the SGS modelling which is the focus of the present work.

The time advancement is by a second-order-accurate Adams–Bashforth scheme (Canuto *et al.* 1988, p. 102), which is popular in LES codes (Moeng 1984; Schmidt & Schumann 1989). The code is run for a long enough time to guarantee that quasi-steady conditions are reached.

For the lower boundary condition given by (2.12), u_* and z_o are taken to be $0.45 \, \text{m s}^{-1}$ and $0.1 \, \text{m}$, respectively. The domain is divided into $N_x \times N_y \times N_z = 54 \times 54 \times 54$ nodes, and additional simulations using the traditional dynamic model are carried out with resolutions of $N_x \times N_y \times N_z = 16 \times 16 \times 16$, $24 \times 24 \times 24$, and $36 \times 36 \times 36$, in order to study the scale dependence of the model coefficient.

The filter width Δ in (2.2) is computed using the common formulation $\Delta = (\Delta_x \Delta_y \Delta_z)^{1/3}$ (Deardorff 1974; Scotti *et al.* 1993), where $\Delta_x = L_x / N_x$ and $\Delta_y = L_y / N_y$. For the traditional Smagorinsky model we choose two sets of parameters: $C_o = 0.1$, $n = 2$; and $C_o = 0.17$, $n = 1$ – values that fall inside the range used by Mason & Thomson (1992) in their simulations.

In order to significantly reduce computational overload, the dynamic coefficients at every horizontal plane are computed only once every 10 time steps. We have found no significant differences in the results by using this reduction.
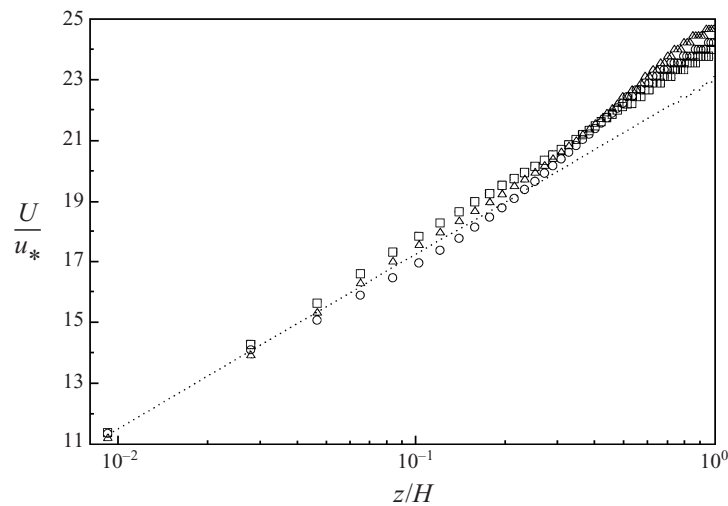
FIGURE 1. Non-dimensional mean streamwise velocity profiles in a semi-logarithmic scale. $\triangle$, Traditional Smagorinsky model with $C_o = 0.1$ and $n = 2$; $\square$, traditional Smagorinsky model with $C_o = 0.17$ and $n = 1$; $\bigcirc$, standard dynamic model. The dotted line corresponds to the classical log-law (expected to hold at $z/H \lesssim 0.1$) with $\kappa = 0.4$.

2.4. *Results*

In a large-eddy simulation, the dissipation characteristics of the model have a direct impact on the turbulent kinetic energy of the resolved field, which in turn affects the shape of the mean velocity profile. Figure 1 shows the mean streamwise velocity profiles obtained from the simulations using the traditional Smagorinsky model (with the two sets of parameters) and the standard dynamic model. In a neutrally stable ABL over a homogeneous surface, the mean streamwise velocity profile is expected to display a logarithmic profile in the lower part (about 10%) of the boundary layer. Thus, below $z/H \sim 0.1$ one would expect better results than those shown in figure 1.

The values of the averaged non-dimensional vertical gradient of the streamwise velocity $\Phi = (\kappa z/u_*)(\mathrm{d}U/\mathrm{d}z)$ resulting from our simulations using the traditional Smagorinsky model and the dynamic Smagorinsky model, are presented as a function of vertical position in figure 2(*a*). As comparison, in figure 2(*b*) we reproduce (with permission) a compilation by Andrén *et al.* (1994) of previous results from four other widely used codes (Mason 1989): eddy-viscosity models with a prognostic equation for the subgrid-scale TKE (Moeng 1984; Nieuwstadt & Brost 1986; Schmidt & Schumann 1989), as well as the Smagorinsky model with backscatter (Mason & Thomson 1992). In all the cases that use the traditional Smagorinsky model, the value of Φ in the near-surface region is substantially larger than the theoretical value of 1, leading to mean velocities larger than predicted by the log-law (see figure 1). This is consistent with the idea that the Smagorinsky model is too dissipative in the near-surface region (Mason 1994), damping the total turbulent kinetic energy to levels that are not large enough to reduce the mean shear in that region. As in figure 1, there is a clear dependence of the results on the choice of the parameters (C_o and n) defining the matching function. The dynamic Smagorinsky model appears to have the opposite effect, i.e. the non-dimensional vertical gradient of the velocity in the near-surface region is smaller than 1. This yields underpredicted mean velocities in the near-surface region (see figure 1). All of the present results deviate less from the
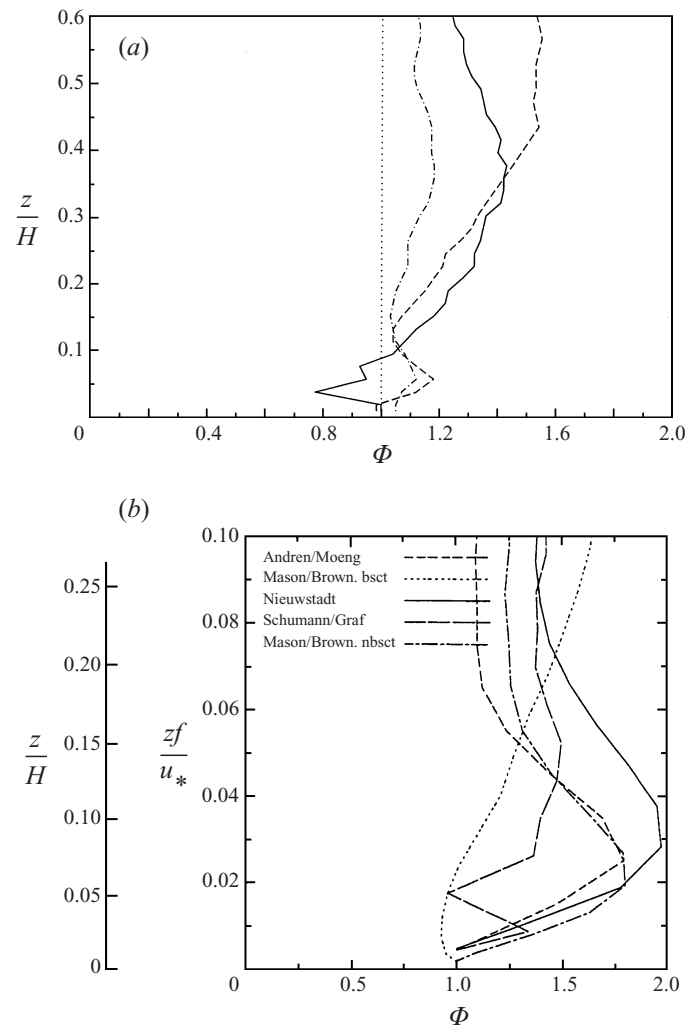
FIGURE 2. (a) Non-dimensional gradient of the mean streamwise velocity ($\Phi = (\kappa z/u_*)(\mathrm{d}U/\mathrm{d}z)$) from simulations with various models. Dashed line: traditional Smagorinsky model with $C_o = 0.1$ and $n = 2$; dot-dashed line: traditional Smagorinsky model with $C_o = 0.17$ and $n = 1$; solid line: standard dynamic model. The dotted line corresponds to the theoretical value of 1 expected in the lower region (about 10%) under neutral conditions. (b) Mean velocity gradients from four widely used LES codes for the ABL as reported by Andrén *et al.* (1994), and reproduced with permission.

ideal log-law in the near-wall region compared to results in figure 2(b) mainly because of the more accurate treatment of the advection term described in the Appendix. In addition to the improvement on the mean velocity, no effect of the modified advection term is found on the second-order statistics (variance of resolved velocity and spectra) reported below.

The vertical distribution of the variance of the three components of the filtered velocity $\langle \widetilde{u}_i'^2 \rangle$ (where $\widetilde{u}_i' = \widetilde{u}_i - \langle \widetilde{u}_i \rangle$) is presented in figures 3(a), 3(b) and 3(c) for $i = 1$, 2, and 3, respectively. In the near-surface region, the traditional Smagorinsky model yields relatively small values of the filtered velocity variances (except for the streamwise component, which is comparable to the dynamic case). This trend is
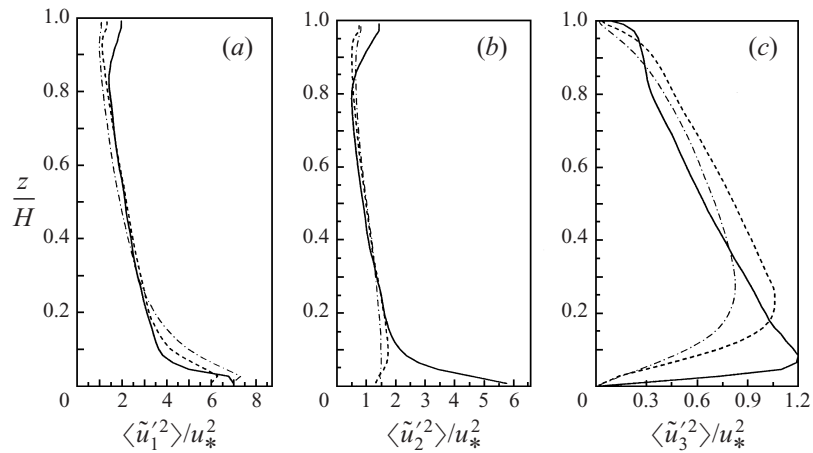
FIGURE 3. Vertical distribution of the normalized variance of the three components of the resolved velocity: (*a*) streamwise $\langle \widetilde{u}_1'^2 \rangle$, (*b*) spanwise $\langle \widetilde{u}_2'^2 \rangle$, (*c*) vertical $\langle \widetilde{u}_3'^2 \rangle$. Dashed line: traditional Smagorinsky model with $C_o = 0.1$ and $n = 2$; dot-dashed line: traditional Smagorinsky model with $C_o = 0.17$ and $n = 1$; solid line: standard dynamic model.

consistent with the high SGS dissipation rate forced by the model in that region, and also with the relatively low values of the resolved TKE. Also evident is the dependence of the results on the choice of the parameters (C_o and n) that define the matching function. The standard dynamic model shows the opposite behaviour. As will be shown later, this is caused by its relatively lower SGS dissipation rate in the near-wall region. This leads to a pile-up of resolved velocity variance (and thus of resolved TKE) in that region.

Figures 4(*a*) and 4(*b*) show the vertical distribution of $\langle \widetilde{u}_1' \widetilde{u}_3' \rangle$, $\langle \tau_{13} \rangle$ and $\langle u_1' u_3' \rangle = \langle \widetilde{u}_1' \widetilde{u}_3' \rangle + \langle \tau_{13} \rangle$, obtained from the simulations using the traditional Smagorinsky model (with $C_o = 0.17$ and $n = 1$) and the standard dynamic model, respectively. The stresses and the height are normalized by u_*^2 and H, respectively. Since the simulations are driven by a constant pressure gradient $\mathrm{d}(P/\rho)/\mathrm{d}x = u_*^2/L_z$ (F_1 in (2.11)), in the absence of viscous stresses, the normalized averaged total turbulent (Reynolds) stress ($\langle u_1' u_3' \rangle / u_*^2$) grows linearly from a value of -1 at the surface to a value of 0 at the top of the boundary layer. The distribution of total shear stresses shown in figures 4(*a*) and 4(*b*) is indeed consistent with the linear behaviour. This result serves as a check of stationarity and momentum conservation of the scheme. Notice that in the near-surface region there is a substantial difference in the relative contribution of the mean SGS stress $\langle \tau_{13} \rangle$ (and thus of the resolved stress) from the two models. The traditional Smagorinsky model yields a SGS stress that is relatively larger near the surface. This, together with the large gradients in the mean velocity field in that region (and thus of $\widetilde{S}_{13}$) shown in figures 1 and 2(*a*), leads to relatively large values of the SGS dissipation of turbulent kinetic energy $\Pi = -\langle \tau_{ij} \widetilde{S}_{ij} \rangle$ (the model is too dissipative). In contrast, the standard dynamic model yields SGS stresses that are relatively small near the surface, associated with low SGS dissipation.

Next, we consider energy spectra. In a neutrally stable ABL, there is experimental evidence that the streamwise velocity spectrum is proportional to $k_1^{-5/3}$ at relatively large wavenumbers ($k_1 \gtrsim z^{-1}$, where z is the measurement height and k_1 is the streamwise wavenumber), consistent with local isotropy of the flow at the small scales. For small wavenumbers ($k_1 \lesssim z^{-1}$), corresponding to large-scale motions (Kader
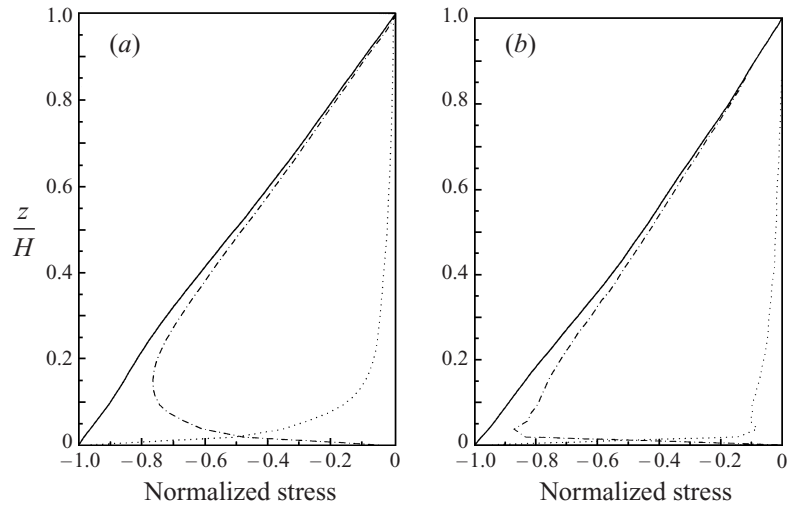
FIGURE 4. Vertical distribution of the mean total and partial (resolved and subgrid-scale) values of the 1, 3 component of the shear stress. The stresses are normalized with u_*^2. Solid line: total turbulent (Reynolds) stress ($\langle u_1' u_3' \rangle$); dotted line; subgrid-scale stress ($\langle \tau_{13} \rangle$); dashed line: resolved stress ($\langle \widetilde{u}_1' \widetilde{u}_3' \rangle$). (a) Traditional Smagorinsky model with $C_o = 0.17$ and $n = 1$. (b) Standard dynamic model.

1984; Kader & Yaglom 1991; Katul *et al.* 1995), the spectrum is proportional to k_1^{-1}. Moreover, Perry, Henbest & Chong (1986) show that the velocity spectra obtained at different positions in fully developed turbulent pipe flow, properly normalized with u_* and z (z is the distance to the pipe wall) collapse when plotted against $k_1 z$ in a log–log scale. The collapsed curves show a clear change in slope, from a value of $-5/3$ at $k_1 z \gtrsim 1$ to a value of -1 at $k_1 z \lesssim 1$.

The averaged streamwise velocity spectra at different heights, obtained from the simulations using the traditional Smagorinsky model with the two sets of parameters and the dynamic Smagorinsky model, are shown in figures 5(a), 5(b) and 5(c), respectively. Spectra are calculated from one-dimensional Fourier transforms of the streamwise velocity component that are then averaged in the horizontal direction and in time. Note that the spectra are normalized with u_* and z and plotted against $k_1 z$, in order to check for a possible collapse of the curves and the change of slope from $-5/3$ to -1. For comparison, in figure 5(d) we reproduce (with permission) the collapse of the spectra obtained experimentally by Perry *et al.* (1986). In figures 5(a) and 5(b), the spectra obtained with the traditional Smagorinsky model decay significantly faster than the expected $(k_1 z)^{-1}$ in the near-wall region. Within the constraints of the pure Smagorinsky model, this type of spectrum means that the model dissipates kinetic energy at an excessive rate. One possible interpretation of this problem is to conclude that a stochastic backscatter of energy term should be added to the model. In this paper, we choose to remain within the framework of the simple Smagorinsky model and explore how much improvement can be gained by determining the coefficient dynamically. In the interior of the flow, the slope of the spectrum is closer to the expected $-5/3$. Also evident is the dependence of the results on the choice of the parameters (C_o and n) that define the matching function of (2.3).

The standard dynamic model (figure 5c), on the other hand, does not involve adjustable parameters but, near the ground, the resulting spectrum decays too slowly, indicating not enough damping. This suggests that the dynamic coefficient may be
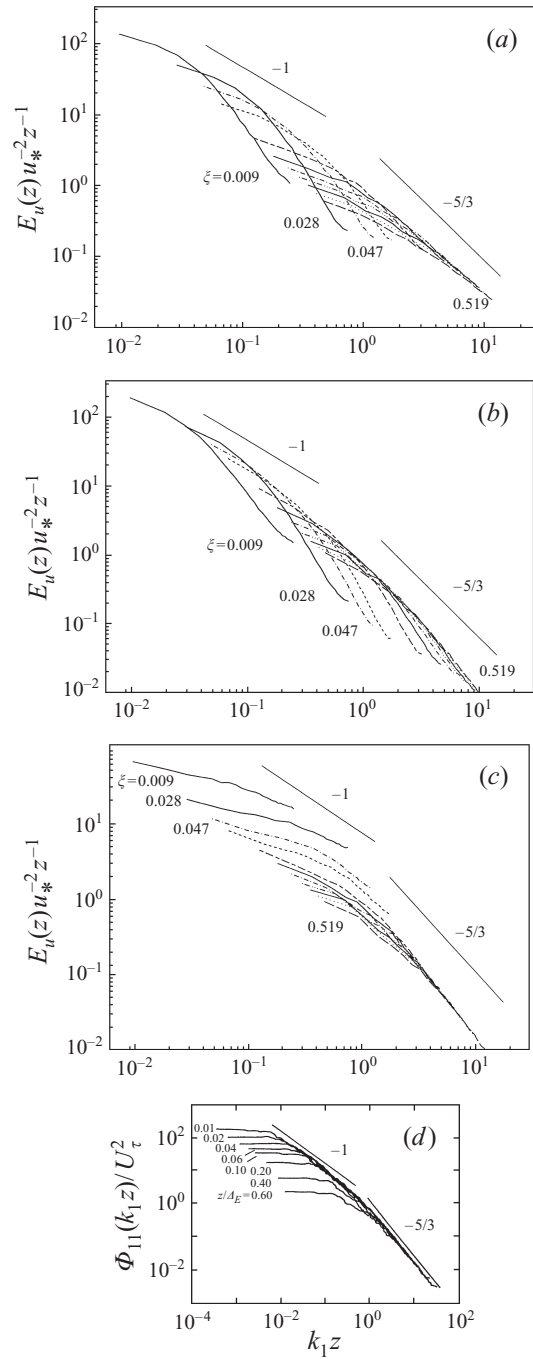
FIGURE 5. Normalized streamwise velocity spectra versus $k_1 z$ at different heights. From top to bottom, the curves are for $\xi = z/H = 0.009, 0.028, 0.047, 0.066, 0.123, 0.179, 0.235, 0.292, 0.349, 0.406, 0.462$ and 0.519. (*a*) Traditional Smagorinsky model with $C_o = 0.1$ and $n = 2$; (*b*) traditional Smagorinsky model with $C_o = 0.17$ and $n = 1$; (*c*) standard dynamic model. The slopes of -1 and $-5/3$ are also shown. (*d*) Velocity spectra obtained in a turbulent pipe ($Re = 2 \times 10^5$, $U_\tau = 1.188$ m s^{-1}) at different positions (z is distance to the pipe wall) as reported by Perry *et al.* (1986).
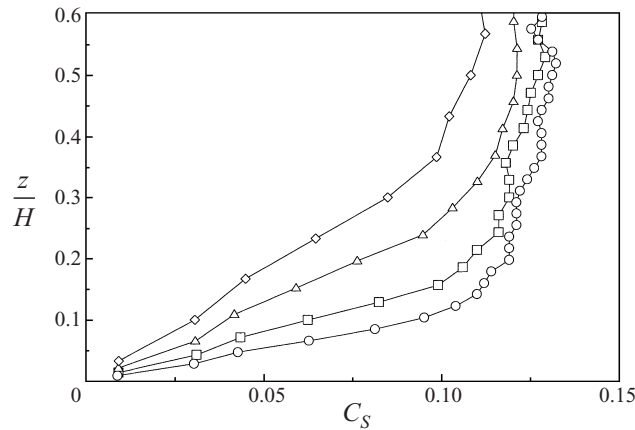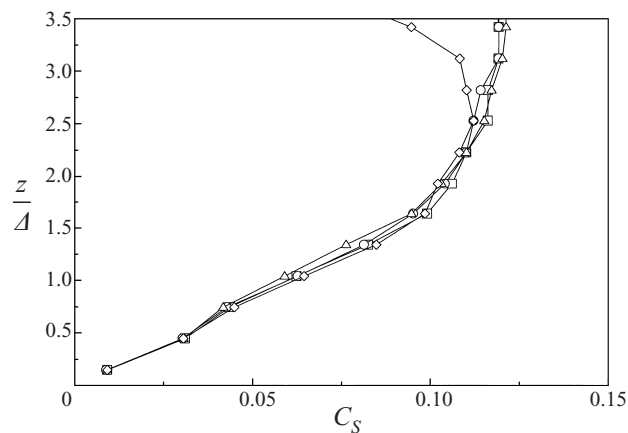
FIGURE 6. Dynamic coefficient as a function of z/H, obtained from simulations with different resolutions: $16 \times 16 \times 16$ nodes ($\diamondsuit$), $24 \times 24 \times 24$ nodes ($\triangle$), $36 \times 36 \times 36$ nodes ($\square$), and $54 \times 54 \times 54$ nodes ($\bigcirc$).

FIGURE 7. Dynamic coefficient as a function of z/Δ, obtained from simulations with different resolutions: $16 \times 16 \times 16$ nodes ($\diamondsuit$), $24 \times 24 \times 24$ nodes ($\triangle$), $36 \times 36 \times 36$ nodes ($\square$), and $54 \times 54 \times 54$ nodes ($\bigcirc$).

too low there. This is likely to be due to the fact that the dynamic procedure samples scales near and beyond the local integral scale, at which turbulence transfer of energy to small scales is weaker, leading to lower values of $\langle L_{ij}M_{ij}\rangle$ and thus to lower coefficients. The lower coefficient then allows pile-up of energy at high wavenumbers. Previous attempts to apply the dynamic model to LES of the ABL have also yielded coefficients that are too low (P. P. Sullivan, C.-H. Moeng, private communication, 1997). Again, in the interior of the flow (away from the wall, where the relative contribution of the non-resolved scales is relatively small and the flow is less anisotropic) the slope of the spectra obtained with the dynamic model is close to the expected $-5/3$.

Next, we document the values of the coefficient returned by the dynamic model. We also examine the dependence of the dynamic coefficient on Δ by applying the traditional dynamic model in four simulations with different resolutions ($16 \times 16 \times 16$, $24 \times 24 \times 24$, $36 \times 36 \times 36$, and $54 \times 54 \times 54$ nodes, respectively). The value of

the dynamic coefficient from the four simulations is presented as a function of the distance to the surface z, normalized by H and by the grid size Δ, in figures 6 and 7, respectively. The collapse of the four curves in figure 7 indicates that the model coefficient C_S is dependent on z/Δ only. Near the ground, we observe the expected $C_S \sim z/\Delta$ behaviour. However, at a fixed height z, this result implies that C_S is a function of Δ.

As pointed out before, the dependence of C_S on Δ is not surprising since the grid scale near the wall approaches the integral scale. However, there is an internal inconsistency in the standard dynamic model in this case since C_S is obtained by assuming scale invariance. Therefore, it is of interest to generalize the dynamic model to include scale dependence.

3. The scale-dependent dynamic model

Next, we proceed to develop a generalization of the dynamic model for applications in which the assumption of (2.6) (scale invariance) is not justified. Without assuming that $C_S(\Delta) = C_S(2\Delta)$ we can still write down the Germano identity for the Smagorinsky model (2.7). However, now M_{ij} is not fully determined but also depends on the ratio of the two coefficients according to (Meneveau & Lund 1997):

$$M_{ij} = 2\Delta^2 \left(\overline{|\widetilde{S}|\widetilde{S}_{ij}} - 4\frac{C_S^2(2\Delta)}{C_S^2(\Delta)} |\overline{\widetilde{S}}|\overline{\widetilde{S}}_{ij} \right). \tag{3.1}$$

Note that this change introduces a new unknown $\beta \equiv C_S^2(2\Delta)/C_S^2(\Delta)$. For scale-invariant situations, $\beta = 1$. Previously, in considering the limit of LES tending to DNS, Meneveau & Lund (1997) proposed using known forms of the viscous range of energy spectra in isotropic turbulence to prescribe non-dynamically an expression for $\beta(\Delta)$, and solve for the coefficient $C_S^2(\Delta)$ dynamically. However, this approach only works when prior knowledge exists about the scale dependence. Hence, such an approach is not truly dynamic.

In order to obtain a dynamic value for β, we employ a second test filter at scale $\widehat{\Delta} > \overline{\Delta}$. For simplicity, and without loss of generality, we take $\widehat{\Delta} = 4\Delta$, and denote variables filtered at scale 4Δ by a caret. Writing the Germano identity between scale Δ and 4Δ yields

$$Q_{ij} - \tfrac{1}{3}\delta_{ij}Q_{kk} = C_S^2 N_{ij}, \tag{3.2}$$

where

$$Q_{ij} = \widehat{\widetilde{u_i \widetilde{u}_j}} - \widehat{\widetilde{u}}_i \widehat{\widetilde{u}}_j, \tag{3.3}$$

and

$$N_{ij} = 2\Delta^2 \left(\widehat{|\widetilde{S}|\widetilde{S}_{ij}} - 4^2 \frac{C_S^2(4\Delta)}{C_S^2(\Delta)} |\widehat{\widetilde{S}}|\widehat{\widetilde{S}}_{ij} \right). \tag{3.4}$$

Again minimizing the error as in §2.2 yields, besides (2.9), another equation for $C_S^2(\Delta)$:

$$C_S^2(\Delta) = \frac{\langle Q_{ij}N_{ij}\rangle}{\langle N_{ij}N_{ij}\rangle}. \tag{3.5}$$

Setting (2.9) equal to (3.5) yields an equation of the form

$$\langle L_{ij}M_{ij}\rangle\langle N_{ij}N_{ij}\rangle - \langle Q_{ij}N_{ij}\rangle\langle M_{ij}M_{ij}\rangle = 0, \tag{3.6}$$

which has two unknowns, $\beta = C_S^2(2\Delta)/C_S^2(\Delta)$ and $\theta = C_S^2(4\Delta)/C_S^2(\Delta)$. Equation (3.6)

is a polynomial in β and θ, since after substitution of the tensors M_{ij} and N_{ij} given by (3.1) and (3.4), we have

$$\langle L_{ij} M_{ij} \rangle = a_1 \beta - b_1, \tag{3.7}$$

$$\langle M_{ij} M_{ij} \rangle = c_1 + d_1 \beta^2 - e_1 \beta, \tag{3.8}$$

$$\langle Q_{ij} N_{ij} \rangle = a_2 \theta - b_2, \tag{3.9}$$

$$\langle N_{ij} N_{ij} \rangle = c_2 + d_2 \theta^2 - e_2 \theta, \tag{3.10}$$

where

$$\left. \begin{aligned} &a_1 = -2\Delta^2 4 \langle |\overline{\overline{S}}|\overline{\overline{S}}_{ij} L_{ij} \rangle, \quad b_1 = -2\Delta^2 \langle |\widetilde{\overline{S}}|\widetilde{\overline{S}}_{ij} L_{ij} \rangle, \\ &c_1 = (2\Delta^2)^2 \langle \overline{|\widetilde{\overline{S}}|\widetilde{\overline{S}}_{ij}} \, \overline{|\widetilde{\overline{S}}|\widetilde{\overline{S}}_{ij}} \rangle, \quad d_1 = (2\Delta^2)^2 4^2 \langle |\overline{\overline{S}}|^2 \overline{\overline{S}}_{ij} \overline{\overline{S}}_{ij} \rangle, \\ &e_1 = 2(2\Delta^2)^2 4 \langle |\overline{\overline{S}}|\overline{\overline{S}}_{ij} \overline{|\widetilde{\overline{S}}|\widetilde{\overline{S}}_{ij}} \rangle, \end{aligned} \right\} \tag{3.11}$$

are also already needed for the traditional dynamic model, and

$$\left. \begin{aligned} &a_2 = -2\Delta^2 4^2 \langle |\widehat{\widetilde{\overline{S}}}|\widehat{\widetilde{\overline{S}}}_{ij} Q_{ij} \rangle, \quad b_2 = -2\Delta^2 \langle \widehat{|\widetilde{\overline{S}}|\widetilde{\overline{S}}_{ij}} Q_{ij} \rangle, \\ &c_2 = (2\Delta^2)^2 \langle \widehat{|\widetilde{\overline{S}}|\widetilde{\overline{S}}_{ij}} \widehat{|\widetilde{\overline{S}}|\widetilde{\overline{S}}_{ij}} \rangle, \quad d_2 = (2\Delta^2)^2 (4^2)^2 \langle |\widehat{\widetilde{\overline{S}}}|^2 \widehat{\widetilde{\overline{S}}}_{ij} \widehat{\widetilde{\overline{S}}}_{ij} \rangle, \\ &e_2 = 2(2\Delta^2)^2 (4)^2 \langle |\widehat{\widetilde{\overline{S}}}|\widehat{\widetilde{\overline{S}}}_{ij} \widehat{|\widetilde{\overline{S}}|\widetilde{\overline{S}}_{ij}} \rangle, \end{aligned} \right\} \tag{3.12}$$

are new terms required for the scale-dependent model.

At this stage we have three unknowns, $C_S(\Delta)$, β and θ, but only two equations, (2.9) and (3.5). Or, more conveniently, (3.6) involving only β and θ and (2.9). In order to close the system, a relationship between β and θ is required. To this end a basic functional form of the scale dependence of the coefficient is postulated. A possible choice is to assume a power law of the form $C_S^2(\Delta) \sim \Delta^\alpha$, or, in a dimensionally appropriate way,

$$C_S^2(\alpha\Delta) = C_S^2(\Delta)\alpha^\phi. \tag{3.13}$$

For a power-law behaviour, β does not depend on scale and is equal to $\beta = 2^\phi$. Note that this assumption is much weaker than the standard dynamic model, which corresponds to the special case $\phi = 0$. We stress that one does not need to assume the power law to hold over a wide range of scales, but only between scales Δ and 4Δ (we have tried another functional form (logarithmic) with negligible effect on the results). A consequence of the assumed local power law is that $C_S^2(2\Delta)/C_S^2(\Delta) = C_S^2(4\Delta)/C_S^2(2\Delta) = \beta$, and thus $\theta = C_S^2(4\Delta)/C_S^2(\Delta) = \beta^2$. With this substitution (3.6) only contains the unknown β, and can be rewritten as follows:

$$P(\beta) \equiv A_0 + A_1\beta + A_2\beta^2 + A_3\beta^3 + A_4\beta^4 + A_5\beta^5 = 0, \tag{3.14}$$

in which

$$\left. \begin{aligned} &A_0 = b_2 c_1 - b_1 c_2, \quad A_1 = a_1 c_2 - b_2 e_1, \quad A_2 = b_2 d_1 + b_1 e_2 - a_2 c_1, \\ &A_3 = a_2 e_1 - a_1 e_2, \quad A_4 = -a_2 d_1 - b_1 d_2, \text{ and } A_5 = a_1 d_2. \end{aligned} \right\} \tag{3.15}$$

The scale-dependent dynamic model thus consists in evaluating the terms A_0, A_1, A_2, A_3, A_4 and A_5 from the filtered velocity at scales 2Δ and 4Δ, finding a physically relevant root of (3.14) (as shown below, there is only one), evaluating M_{ij} from (3.1) and finally obtaining the required grid-scale coefficient from (2.9). The next section presents an application of this model to LES of the neutral atmospheric boundary layer considered in §2.3.
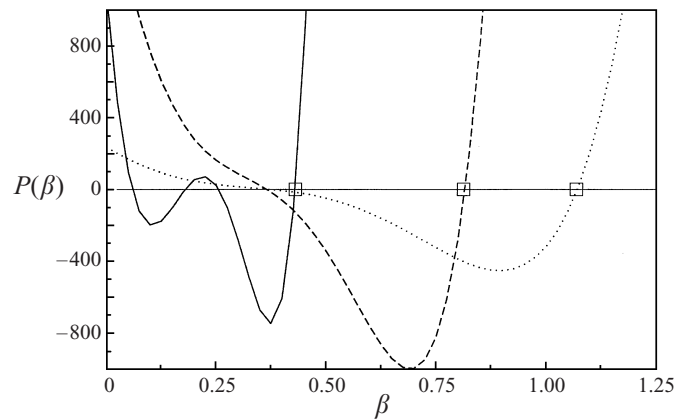
FIGURE 8. Polynomial $P(\beta) = A_0 + A_1\beta + A_2\beta^2 + A_3\beta^3 + A_4\beta^4 + A_5\beta^5$, as a function of β at different heights z. Solid line: $z = \Delta_z/2$; dashed line: $z = H/4$; dotted line: $z = H/2$. For presentation purposes, the polynomials have been scaled by multiplying by 10^{-11}, 10^{-6}, and 10^{-6}, respectively. The squares correspond to the largest root (value used in the simulation).

4. Application and results

The scale-dependent model is implemented in the simulation of a neutral ABL. Numerical details are as described in §2.3. The additional test-filtered quantities at scale 4Δ are obtained by spectral cutoff filtering in the (x, y)-planes. As in the traditional dynamic model, tensor contractions are averaged over such planes, corresponding to a minimization of the error in the modelled Germano identity over these regions of statistical homogeneity (Ghosal *et al.* 1995). Three resolutions have been used: $24 \times 24 \times 24$, $36 \times 36 \times 36$, and $54 \times 54 \times 54$ nodes. The $54 \times 54 \times 54$-nodes simulation is taken as a base case to present the results. Some results from the other two resolutions are also presented to illustrate the independence of the results on grid size.

4.1. *Scale dependence of the model parameter*

Figure 8 shows a family of fifth-order polynomials in β obtained during the simulation using (3.14). Different lines show results for different heights at a single time. As can be seen, there is a series of possible roots for the polynomial. However, only the largest root is physically meaningful, since the other values of β are associated with changes in sign of $\langle L_{ij}M_{ij}\rangle$ and/or $\langle Q_{ij}N_{ij}\rangle$. From (3.1) and (3.4), it is evident that a decrease in β (and therefore in θ) from an initial value of 1 implies a decrease in $\langle L_{ij}M_{ij}\rangle$ and $\langle Q_{ij}N_{ij}\rangle$ that eventually leads to a change in the sign of one or both of these quantities. Negative values of $\langle L_{ij}M_{ij}\rangle$ and/or $\langle Q_{ij}N_{ij}\rangle$ are physically not meaningful since they correspond to negative eddy viscosities. In figure 9 the value of the coefficient (only positive values are shown), computed using test filters of size 2Δ (equation (2.9)) and 4Δ (equation (3.5)), respectively, are plotted as a function of β, corresponding to the same heights and times used in figure 8. The two curves intersect only for the values of β corresponding to the largest root of the polynomial (see figure 8). In order to solve the polynomial equations for β (3.14), a Newton–Raphson technique is employed, with a starting point at a value of β significantly larger than 1 (we use $\beta_o = 6$). We note that, occasionally, β can assume instantaneous values larger than 1 (before time averaging).

In terms of computational speed, with the dynamic procedure applied every 10 time steps, we found the standard and scale-dependent dynamic models to take only
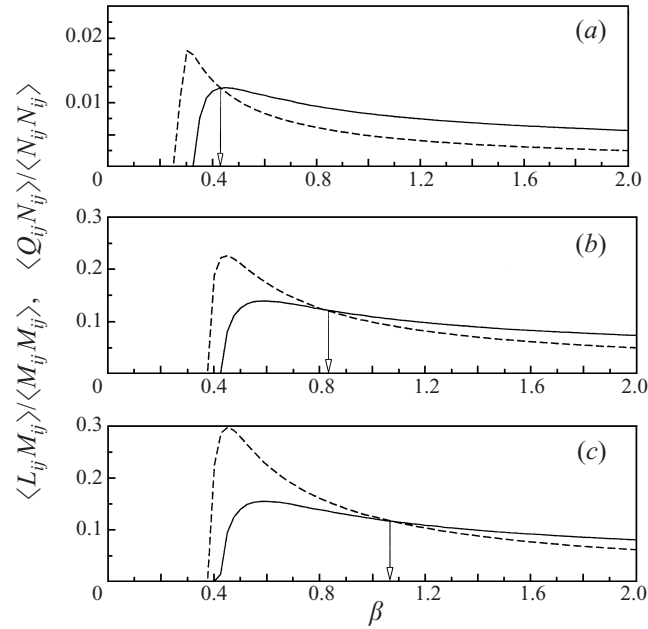
FIGURE 9. Model coefficient computed using the dynamic procedure with test filters of sizes 2Δ (equation (2.9)) (solid line) and 4Δ (equation (3.5)) (dashed line) as a function of β at different heights z. (a) $z = \Delta_z/2$; (b) $z = H/4$; (c) $z = H/2$. The arrows point to the value of the largest root of the polynomials in figure 8.
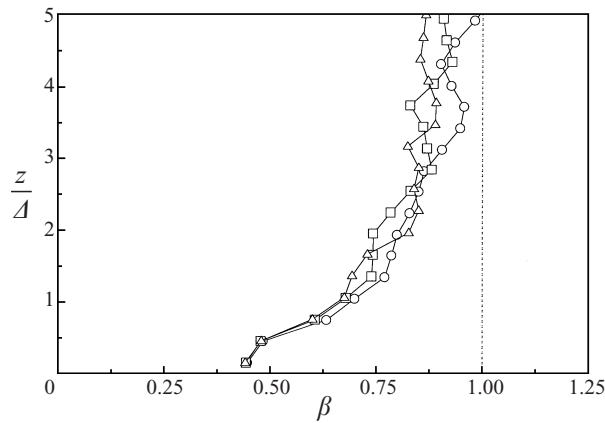

FIGURE 10. Vertical distribution of the time-averaged value of β, obtained using the scale-dependent dynamic model with three different resolutions: $24 \times 24 \times 24$ nodes ($\triangle$), $36 \times 36 \times 36$ nodes ($\square$), and $54 \times 54 \times 54$ nodes ($\bigcirc$). The height z is normalized with the filter size Δ.

about 4% and 8% more CPU time, respectively, than the traditional Smagorinsky model. The root-finding procedure to solve for β is performed only once for each plane and thus does not add significantly to the CPU time.

The time-averaged values of β, obtained by solving (3.14) are presented in figure 10 as a function of the normalized height z/Δ for three different resolutions. Note the collapse of the curves, indicating that β also depends on z/Δ. In the scale-dependent dynamic model it is assumed that β is independent of Δ, while the present results
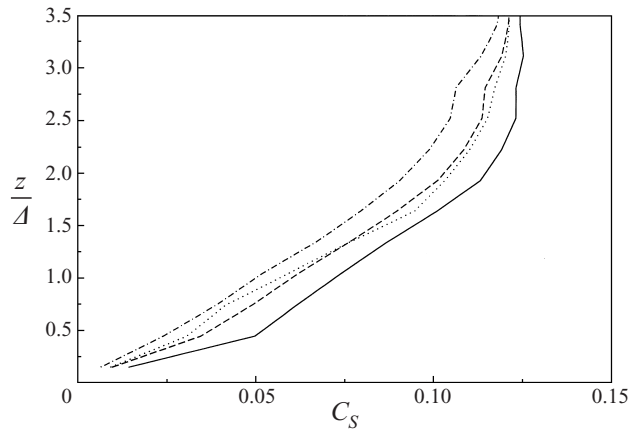
FIGURE 11. Vertical distribution of the time-averaged value of the coefficients $C_S(\Delta)$ (solid line), $C_S(2\Delta)$ (dashed line), and $C_S(4\Delta)$ (dot-dashed line), obtained using the scale-dependent dynamic model. The dotted line corresponds to the value of the coefficient obtained using the traditional dynamic model.

show that β also varies with Δ. Note however that the variation in β is a higher-order effect and is significantly weaker than variations of $C_S(\Delta)$ which tends to zero near the wall instead of to a finite value. In the interior of the flow the value of β is close to 1, indicating that $C_S^2(4\Delta) \approx C_S^2(2\Delta) \approx C_S^2(\Delta)$, which is consistent with the fact that Δ is well within the inertial range of turbulence in that region. The decrease of β from the value of 1 (corresponding to scale invariance) as the ground is approached is consistent with the idea that $C_S^2(4\Delta) < C_S^2(2\Delta) < C_S^2(\Delta)$, as shown in §2.4. Figure 11 shows the vertical distribution of the average value of the resulting coefficients $C_S(\Delta)$, $C_S(2\Delta) = \beta^{1/2}C_S(\Delta)$, and $C_S(4\Delta) = \beta C_S(\Delta)$, all obtained using the scale-dependent procedure. Also shown is the average value of the coefficient that results from the traditional dynamic model ((2.9) with $\beta = 1$). Interestingly, the latter value is closest to the profile for the test-filter scale coefficient $C_S(2\Delta)$, i.e. the traditional dynamic model gives the coefficient appropriate to the test-filter scale (which in this application is too low). A similar trend was also found for the transition to the viscous range in Meneveau & Lund (1997).

The $24 \times 24 \times 24$ and $36 \times 36 \times 36$ simulations are uniformly robust over arbitrary long simulation times. In the $54 \times 54 \times 54$-nodes simulation, we occasionally find that some instability develops in the uppermost part of the domain near the stress-free boundary. It yields relatively large values of β, associated with small values of $C_S(\Delta)$ and a pile-up of kinetic energy at the higher wavenumbers of the velocity spectrum. This instability does not extend to the lower half of the domain, where the results remain unaltered. The instability disappears when three-dimensional test filters are used in the upper region, suggesting that it is associated with a decoupling of the dynamics between horizontal planes in the near-top region. The effect of filter dimensionality on the development of such instabilities near the upper boundary is left for future investigations.

4.2. *Mean quantities*

The mean streamwise velocity profile from the three simulations with the scale-dependent dynamic model is presented in semi-logarithmic scales in figure 12, together with the results from the standard dynamic model. In the near-surface region (lower
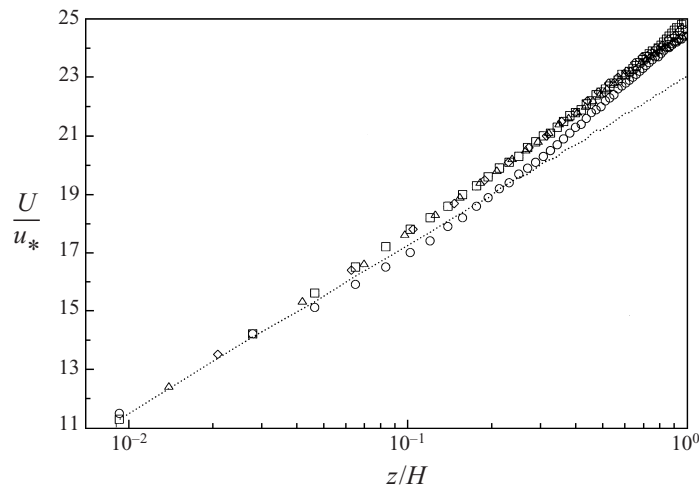
FIGURE 12. Non-dimensional mean streamwise velocity profiles in a semi-logarithmic scale. Standard dynamic model: ($\bigcirc$); scale-dependent model at three resolutions: $24 \times 24 \times 24$ nodes ($\diamondsuit$), $36 \times 36 \times 36$ nodes ($\triangle$), and $54 \times 54 \times 54$ nodes ($\square$). The dotted line corresponds to the classical log-law (expected to hold in the lower 10% of the domain) with $\kappa = 0.4$.
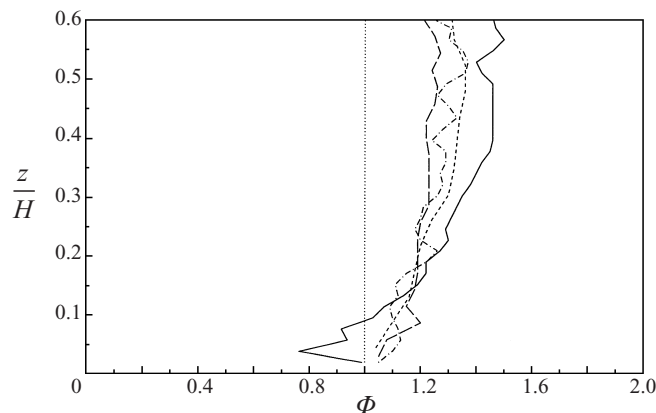

FIGURE 13. Non-dimensional gradient of the mean streamwise velocity ($\Phi = (\kappa z/u_*)(\mathrm{d}U/\mathrm{d}z)$) from simulations that use the scale-dependent model at three resolutions: $24 \times 24 \times 24$ nodes (short-dashed line); $36 \times 36 \times 36$ nodes (long-dashed line); and $54 \times 54 \times 54$ nodes (dot-dashed line) compared to the standard dynamic model (solid line). The dotted line corresponds to the classical log-law (expected to hold in the lower 10% of the domain) with $\kappa = 0.4$.

10% of the domain), the resulting mean velocity profile from the scale-dependent model is closer to the expected log-law behaviour (straight line) than is the standard dynamic model. The averaged non-dimensional velocity gradient $\Phi = (\kappa z/u_*)(\mathrm{d}U/\mathrm{d}z)$ from the scale-dependent dynamic model and the standard dynamic model is shown in figure 13. The scale-dependent dynamic model yields a value of Φ that remains closer to 1 and relatively constant near the wall, indicative of the expected logarithmic velocity profile, and increases progressively as we move away from the wall into the so-called wake region. As shown in figures 12 and 13, the mean velocity profile obtained using the scale-dependent dynamic model is not affected by changes in resolution.
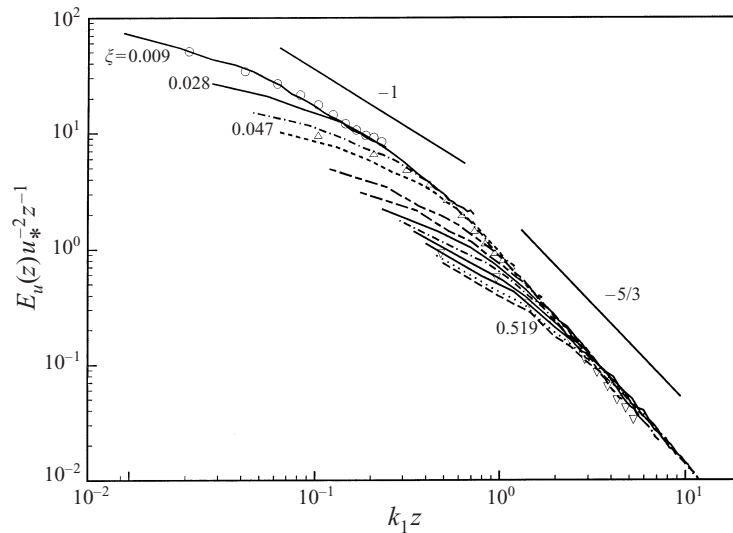
FIGURE 14. Normalized streamwise velocity spectra versus $k_1 z$ at different heights, using the proposed scale-dependent dynamic model at two resolutions: $54 \times 54 \times 54$ nodes (lines as in figure 5) and $24 \times 24 \times 24$ nodes ($\xi = z/H = 0.021$ ($\bigcirc$); $\xi = 0.104$ ($\triangle$); and $\xi = 0.438$ ($\diamondsuit$). The slopes of -1 and $-5/3$ are also shown.

4.3. *Second-order moments*

The averaged streamwise velocity spectra obtained from the $54 \times 54 \times 54$-nodes simulation using the scale-dependent model at different positions (z) in the ABL are shown in figure 14. Also, spectra corresponding to three different heights in the $24 \times 24 \times 24$-nodes simulation are plotted in figure 14 to illustrate the grid independence of the results. As before, the spectra are normalized with u_* and z. Figure 14 shows good agreement with the experimental results of Perry *et al.* (1996) (see figure 5*d*), with a clear collapse of the spectra and the change of slope near $k_1 z \approx 1$. As an example, consider a comparison between the $\xi = 0.009$ curve nearest to the wall in figures 5(*c*) and 14, with the $\xi = z/\Delta_E = 0.01$ curve in figure 5(*d*). The latter has an approximately k^{-1} behaviour down to $k_1 z \approx 10^{-2}$ and then becomes flat at the lowest wavenumbers. In the standard dynamic model results of figure 5(*c*) this curve is clearly much flatter than k^{-1}, in a range of $k_1 z$ values between 10^{-2} and 10^{-1}, where the true behaviour (figure 5*d*) should be k_1^{-1}. Figure 14 with the scale-dependent model shows approximately a k_1^{-1} scaling for this curve, and very clearly a collapse with the other curves. Also visible is the flattening at low wavenumbers, although more gradual than in figure 5(*d*). Similar arguments apply to the other curves at greater distances from the wall, which now begin to include the $-5/3$ range as well. Excellent agreement is also observed with similar trends presented in Kader & Yaglom (1991, figure 3). This result suggests that near the surface the scale-dependent model is able to better reproduce the rate of dissipation of turbulent kinetic energy towards the subgrid scales than the Smagorinsky and standard dynamic models, which are too dissipative and not dissipative enough, respectively (compare with figures 5*a*, 5*b* and 5*c*). We conclude that allowing for scale dependence in the dynamic model leads to improved prediction of the local turbulence statistics.

The vertical distribution of the variance of the three components of the filtered velocity $\langle \widetilde{u}_i'^2 \rangle$ is presented in figures 15(*a*), 15(*b*) and 15(*c*) for $i = 1, 2$, and 3,
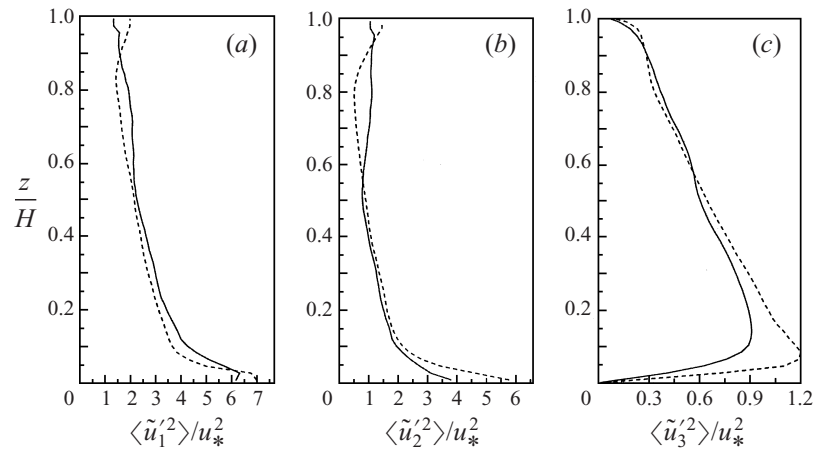
FIGURE 15. Vertical distribution of the variance of the three components of the resolved velocity. (*a*) Streamwise $\langle \tilde{u}_1'^2 \rangle$, (*b*) spanwise $\langle \tilde{u}_2'^2 \rangle$, (*c*) vertical $\langle \tilde{u}_3'^2 \rangle$. Dashed line: standard dynamic model; solid line: scale-dependent dynamic model.
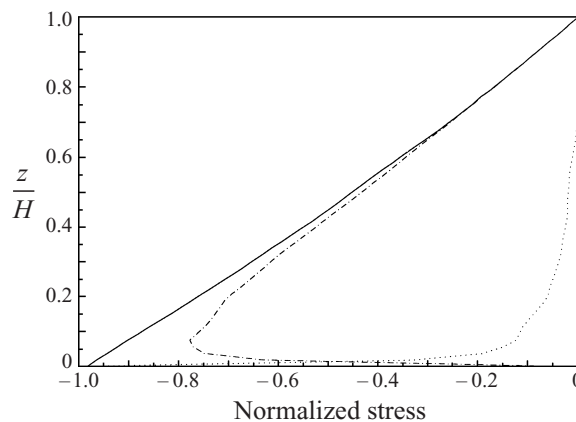

FIGURE 16. Vertical distribution of the mean total and partial (resolved and subgrid-scale) values of the 1, 3 component of the shear stress, obtained using the scale-dependent dynamic model. The stresses are normalized with u_*^2. Solid line: total turbulent (Reynolds) stress ($-\langle u_1' u_3' \rangle$); dotted line: subgrid-scale stress ($\langle \tau_{13} \rangle$); dashed line: resolved stress ($\langle \tilde{u}_1' \tilde{u}_3' \rangle$).

respectively. In the near-surface region, the scale-dependent dynamic model yields filtered velocity variances which fall between the values obtained with the standard dynamic model and the traditional Smagorinsky model (see also figures 3*a*, 3*b* and 3*c*).

Figure 16 shows the vertical distribution of the mean total and partial (resolved and subgrid-scale) values of the normalized shear stress. In the near-surface region, the scale-dependent model yields mean SGS stress $\langle \tau_{13} \rangle$ that is smaller than the traditional Smagorinsky model (figure 4*a*) and larger than the standard dynamic model (figure 4*b*).

5. Conclusions

A generalization of the dynamic model that allows the coefficient to change with $\varDelta$ in a self-consistent fashion is proposed. The new model involves introducing a

secondary test filter that, together with the traditional test filter, is used to determine both the coefficient and how it changes across scales. A general local power-law variation for $C_S(\Delta)$ is assumed for the scale dependence in the vicinity of Δ. Note that this assumption is far weaker than the scale invariance of the traditional dynamic model. Now one must solve for two unknown parameters: $C_S(\Delta)$ and the exponent ϕ of the power law (or the ratio $\beta = 2^{\phi}$). The scale-dependent dynamic model, together with the traditional Smagorinsky and standard dynamic models, are applied to LES of a neutrally stable atmospheric boundary layer. Using different filter sizes Δ, we show that the dynamic coefficient obtained from the traditional dynamic procedure depends on the ratio z/Δ, implying scale dependence at any fixed z. This strongly motivates the use of the new scale-dependent dynamic model in LES of ABL flows.

Velocity spectra from simulations that use the proposed scale-dependent model show that the new model improves the predictions of spectral slopes at different heights from the ground. In the near-surface region, the traditional Smagorinsky and traditional dynamic models are too dissipative and not dissipative enough, respectively. Consistent with its improved dissipation characteristics, the scale-dependent model also yields improved profiles of mean velocity.

In summary, the basic conclusions from this paper are: (1) the dynamic model can be generalized to allow for scale dependence in a fully dynamic and self-consistent way; (2) simulations with such a model are stable and robust, and yield expected trends of the coefficient as function of scale; (3) applications to LES of the ABL show improved dissipative properties of the model, leading to more realistic spectra and mean velocity profiles.

Our calculations show that the improvement of the SGS model clearly improves results even when the classical (possibly defficient) wall-stress boundary condition is used. Such an improved understanding of the isolated effect of the SGS model on the results is very important when addressing the issue of the boundary condition. As reviewed by Piomelli (1999), the log-layer-based approach has well-known limitations and there is currently a growing interest in improving it for, among others, predicting pressure gradient effects and separation at high Reynolds numbers. Several of the current efforts attempt to merge smoothly between an LES approach in the bulk of the flow, and a Reynolds-averaged approach in the near-wall region. In that context, by explicitly allowing for scale dependence near the edge of the inertial range, the proposed scale-dependent dynamic model may well extend the applicability of the dynamic model from the LES region towards any possible overlap region with RANS near the wall.

Future work should extend the implementation of the scale-dependent dynamic procedure to other base models (e.g. mixed model, Lagrangian dynamic model), and to other flows where scale dependence of the model coefficient can be expected. Examples include turbulence undergoing rapid distortion, flows with stratification, compressible and reacting flows.

Appendix

The $\widetilde{u}_3 \partial \widetilde{u}_1 / \partial z$ convective term near the ground is treated in a special fashion. This improvement is motivated by the fact that the vertical derivative of an expected logarithmic mean profile diverges at the wall, causing some errors in the finite-difference approximation there.

The values of $\widetilde{u}_3$ and $\partial \widetilde{u}_1 / \partial z$ are obtained at the $\widetilde{u}_3$-nodes in the staggered grid, placed at $z = (\delta - 1)\Delta_z$ (with $1 < \delta < N_z$). For a logarithmic mean velocity profile, the exact value of the vertical derivative of the mean streamwise velocity diverges as z^{-1}:

$$\left[\frac{\partial U(z)}{\partial z} \right]_{ex} = \frac{u_*}{\kappa} \frac{1}{z}, \tag{A 1}$$

where $U(z) = \langle \widetilde{u}_1 \rangle$ is the mean streamwise velocity at height z. The finite-difference approximation of that derivative

$$\left[\frac{\partial U(z)}{\partial z} \right]_{fd} = \frac{1}{\Delta_z}(U(z + \tfrac{1}{2}\Delta_z) - U(z - \tfrac{1}{2}\Delta_z)) \tag{A 2}$$

combined with the logarithmic mean velocity profile,

$$U(z) = \frac{u_*}{\kappa} \ln(z/z_o), \tag{A 3}$$

yields

$$\left[\frac{\partial U(z)}{\partial z} \right]_{fd} = \frac{1}{\Delta_z} \frac{u_*}{\kappa} \ln\left(\frac{z + \tfrac{1}{2}\Delta_z}{z - \tfrac{1}{2}\Delta_z} \right). \tag{A 4}$$

The ratio between the exact value of the derivative (given by A1) and the finite-difference approximation (given by A4) is

$$f = \frac{\Delta_z}{z} \left[\ln\left(\frac{z + \tfrac{1}{2}\Delta_z}{z - \tfrac{1}{2}\Delta_z} \right) \right]^{-1}. \tag{A 5}$$

Notice that the error incurred by using the finite-difference approximation is relatively large at $z = \Delta_z$ ($f = (\ln(3))^{-1} \simeq 0.91$, i.e. an error of 9%) but it rapidly decreases (f is very close to 1) as we move upwards.

In order to account for the error incurred by using the finite-difference approximation, the value of the derivative $\partial \widetilde{u}_1 / \partial x_3$ at $z = \Delta_z$ is corrected using

$$\frac{\partial \widetilde{u}_1}{\partial z} = \left[\frac{\partial \widetilde{u}_1}{\partial z} \right]_{fd} + \frac{\partial U(z)}{\partial z}(1 - (\ln(3))^{-1}). \tag{A 6}$$

This correction is not applied to the value of the derivative at higher levels (above $z = \Delta_z$) because there the error is negligible. Simulations show that this correction only improves the mean velocity profile in the lower levels of nodes for all model cases considered in this paper. It appears to have no effect on the resolved kinetic energy levels and the SGS dissipation rate from the simulations, and no change in velocity spectra and variance of the resolved velocity fields is observed.

REFERENCES

ALBERTSON, J. D. & PARLANGE, M. B. 1999 Natural integration of scalar fluxes from complex terrain. *Adv. Water Resour.* **23**, 239–252.

ANDRÉN, A., BROWN, A. R., GRAF, J., MASON, P. J., MOENG C.-H., NIEUWSTADT, F. T. M. &

SCHUMANN, U. 1994 Large-eddy simulation of the neutrally stratified boundary layer: A comparison of four computer codes. *Q. J. R. Metl. Soc.* **120**, 1457–1484.

BALARAS, E., BENOCCI, C. & PIOMELLI, U. 1995 Finite-difference computations of high Reynolds number flows using the dynamic subgrid-scale model. *Theor. Comput. Fluid Dyn.* **7**, 207–216.

BARDINA, J. 1983 Improved turbulence models based on large eddy simulation of homogeneous, incompressible, turbulent flows. PhD thesis; Rep. TF-19: Mechanical Engineering, Stanford University.

BARDINA, J., FERZIGER, J. H. & REYNOLDS, W. C. 1980 Improved subgrid scale models for large eddy simulation. *AIAA Paper* 80–1357.

BUSINGER, J. A., WYNGAARD, J. C., IZUMI, Y. & BRADLEY, E. F. 1971 Flux-profile relationships in the atmospheric surface layer. *J. Atmos. Sci.* **28**, 181–189.

CANUTO, C., HUSSAINI, M. Y., QUARTERONI, A. & ZANG, T. A. 1988 *Spectral Methods in Fluid Dynamics* Springer.

CANUTO, V. M. & MINOTTI, F. 1993 Stratified turbulence in the atmosphere and oceans: a new subgrid model. *J Atmos. Sci.* **50**, 1925–1935.

DEARDORFF, J. W. 1970 A numerical study of three-dimensional turbulent channel flow at large Reynolds numbers. *J. Fluid Mech.* **41**, 453–480.

DEARDORFF, J. W. 1974 Three dimensional numerical study of turbulence in an entraining mixed layer. *Boundary-Layer Met.* **7**, 199–226.

GERMANO, M., PIOMELLI, U., MOIN, P. & CABOT, W. 1991 A dynamic subgrid-scale eddy viscosity model. *Phys. Fluids* A **3**, 1760–1765.

GHOSAL, S., LUND, T. S., MOIN, P. & AKSELVOLL, K. 1995 A dynamic localization model for large-eddy simulation of turbulent flows. *J. Fluid Mech.* **286**, 229–255.

GHOSAL, S. & MOIN, P. 1995 The basic equations for the large eddy simulation of turbulent flows in complex geometries. *J. Comput. Phys.* **186**, 24–37.

GROTZBACH, G. & SCHUMANN, U. 1977 Direct numerical simulation of turbulent velocity, pressure-and temperature-fields in channel flows. *Symposium on Turbulent Shear Flows, The Pennsylvania State University, April 18–20* (ed. F. Durst *et al.*). Springer.

HORIUTI, K. 1993 A proper velocity scale for modelling subgrid-scale eddy viscosities in large-eddy simulation. *Phys. Fluids* A **5**, 146–157.

HORIUTI, K. 1997 A new dynamic two-parameter mixed model for large-eddy simulation. *Phys. Fluids* **9**, 3443–3464.

KADER, B. A. 1984 Structure of anisotropic velocity and temperature fluctuations in a developed turbulent boundary layer. *Izv. Akad. Nauk SSSR, Meckh. Zhidk. i Gaza* **4**, 47–56.

KADER, B. A. & YAGLOM, A. M. 1991 Spectra and correlation functions of surface layer atmospheric turbulence in unstable thermal stratification. *In Turbulence and Coherent Structures* (ed. O. Métais & M. Lesieur) Kluwer.

KATUL, G. G., CHU, C. R., PARLANGE, M. B., ALBERTSON, J. D. & ORTENBURGER, T. A. 1995 Low-wavenumber spectral characteristics of velocity and temperature in the atmospheric boundary layer. *J. Geophys. Res.* **100**, 14243–14255.

KHANNA, S. & BRASSEUR, J. G. 1997 Analysis of Monin–Obukhov similarity from large-eddy simulation. *J. Fluid Mech.* **345**, 251–286.

LESIEUR, M. & MÉTAIS, O. 1996 New trends in large-eddy simulations of turbulence. *Ann. Rev. Fluid Mech.* **28**, 45–82.

LILLY, D. K. 1967 The representation of small-scale turbulence in numerical simulation experiments. In *Proc. IBM Scientific Computing Symposium on Environmental Sciences*, p. 195.

LILLY, D. K. 1992 A proposed modification of the Germano subgrid-scale closure method. *Phys. Fluids* A **4**, 633–635.

LIU, S., KATZ, J. & MENEVEAU, C. 1999 Evolution and modelling of subgrid scales during rapid straining of turbulence. *J. Fluid Mech.* **387**, 281–320.

LIU, S., MENEVEAU, C. & KATZ, J. 1994 On the properties of similarity subgrid-scale models as deduced from measurements in a turbulent jet. *J.Fluid Mech.* **275**, 83–119.

MASON, P. J. 1989 Large-eddy simulation of the convective atmospheric boundary layer. *J. Atmos. Sci.* **46**, 1492–1516.

MASON, P. 1994 Large-eddy simulation: a critical review of the technique. *Q. J. R. Metl. Soc.* **120**, 1–26.

Mason, P. J. & Thomson, D. J. 1992 Stochastic backscatter in large-eddy simulations of boundary layers. *J. Fluid Mech.* **242**, 51–78.

Meneveau, C. & Katz, J. 2000 Scale-invariance and turbulence models for large-eddy simulation. *Ann. Rev. Fluid Mech.* **32**, 1–32.

Meneveau, C. & Lund T. S. 1997 The dynamic Smagorinsky model and scale-dependent coefficients in the viscous range of turbulence. *Phys. Fluids* **9**, 3932–3934.

Meneveau, C., Lund, T. & Cabot, W. 1996 A Lagrangian dynamic subgrid-scale model of turbulence. *J Fluid Mech.* **319**, 353–385.

Moeng, C.-H. 1984 A large-eddy simulation model for the study of planetary boundary-layer turbulence. *J. Atmos. Sci.* **46**, 2311–2330.

Moeng, C.-H. & Wyngaard, J. C. 1984 Statistics of conservative scalars in the convective boundary layer. *J. Atmos. Sci.* **41**, 3161–3169.

Moin, P. & Kim, J. 1982 Numerical investigation of turbulent channel flow. *J. Fluid Mech.* **118**, 341–377.

Nieuwstadt, F. T. M. & Brost, R. A. 1986 The decay of convective turbulence. *J. Atmos. Sci.* **43**, 532–546.

Orszag, S. A. 1970 Transform method for calculation of vector coupled sums: Application to the spectral form of the vorticity equation. *J. Atmos. Sci.* **27**, 890–895.

Orszag, S. A. & Pao, Y.-H. 1974 Numerical computation of turbulent shear flows. *Adv. Geophys.* **18** A, 224–236.

Ozmidov, R. V. 1975 On the turbulent exchange in a stably stratified ocean. *Izv. Acade. Sci. USSR, Atmos. Ocean Phys.* **1**, 493–497.

Perry, A. E., Henbest, S. & Chong, M. S. 1986 A theoretical and experimental study of wall turbulence. *J. Fluid Mech.* **165**, 163–199.

Piomelli, U. 1993 High Reynolds number calculations using the dynamic subgrid-scale stress model. *Phys. Fluids* A **5**, 1484–1490.

Piomelli, U. 1999 Large-eddy simulation: achievements and challenges. *Prog. Aerospace Sci.* **35**, 335–362.

Piomelli, U., Moin, P. & Ferziger, J. H. 1988 Model consistency in large eddy simulation of turbulent channel flows. *Phys. Fluids* **31**, 1884–1891.

Piomelli, U., Yu, Y. & Adrian, R. J. 1996 Subgrid-scale energy transfer and near-wall turbulence structure. *Phys. Fluids* **8**, 215–224.

Pope, S. B. 2000 *Turbulent Flows.* Cambridge University Press.

Sarghini, F., Piomelli, U. & Balaras, E. 1998 Scale-similar models for large-eddy simulations. *Phys. Fluids* **11**, 1596–1607.

Schmidt, H. & Schumann, U. 1989 Coherent structure of the convective boundary layer derived from large-eddy simulation. *J. Fluid Mech.* **200**, 511–562.

Schumann, U. 1975 Subgrid scale model for finite difference simulations of turbulent flows in plane channels and annuli. *J. Comput. Phys.* **18**, 376–404.

Schumann, U. 1995 Stochastic backscatter of turbulence energy and scalar variance by random subgrid-scale fluxes. *Proc. R. Soc. Lond.* A **451**, 293–318.

Schumann, U., Grotzbach, G. & Kleiser, L. 1980 Direct numerical simulation of turbulence. *In Prediction Methods for Turbulent Flows* (ed. W. Kollmann). Hemisphere.

Scotti, A., Meneveau, C. & Lilly, D. K. 1993 Generalized Smagorinsky model for anisotropic grids. *Phys. Fluids* **5**, 2306–2308.

Shaw, R. H. & Schumann, U. 1992 Large-eddy simulation of turbulent flow above and within a forest. *Boundary-Layer Metl.* **61**, 47–64.

Smagorinsky, J. 1963 General circulation experiments with the primitive equations, Part 1: the basic experiment. *Mon. Weath. Rev.* **91**, 99–164.

Smith, L. M. & Yakhot, V. 1993 Short- and long-time behaviour of eddy-viscosity models. *Theor. Comput. Fluid Dyn.* **4**, 197–207.

Sullivan, P. P., McWilliams J. C. & Moeng, C.-H. 1994 A subgrid-scale model for large-eddy simulation of planetary boundary-layer flows. *Boundary-Layer Met.* **71**, 247–276.

Voke, P. R. 1996 Subgrid-scale modelling at low mesh Reynolds number. *Theor. Comput. Fluid Dyn.* **8**, 131–143.